The Astrophysical Journal, 953:3 (8pp), 2023 August 10 https://doi.org/10.3847/1538-4357/acdfd2

Are Nonthermal Velocities in Active Region Coronal Loops Anisotropic?

Michael Hahn[1], Mahboubeh Asgari-Targhi[2], and Daniel Wolf Savin[1]
[1] Columbia Astrophysics Laboratory, Columbia University, 550 West 120th Street, New York, NY 10027, USA; mhahn@astro.columbia.edu
[2] Harvard-Smithsonian Center for Astrophysics, 60 Garden Street MS-15, Cambridge, MA 02138, USA
Received 2023 April 27; revised 2023 June 2; accepted 2023 June 13; published 2023 July 28

Abstract

We have measured line widths in active region coronal loops in order to determine whether the nonthermal broadening is anisotropic with respect to the magnetic field direction. These nonthermal velocities are caused by unresolved fluid motions. Our analysis method combines spectroscopic data and a magnetic field extrapolation. We analyzed spectra from the Extreme Ultraviolet Imaging Spectrometer on Hinode. A differential emission measure analysis showed that many spectral lines that are commonly considered to be formed in the active region have a substantial contribution from the background quiet Sun. From these spectra we identified lines whose emission was dominated by the active region loops rather than background sources. Using these lines, we constructed maps of the nonthermal velocity. With data from the Helioseismic Magnetic Imager on the Solar Dynamics Observatory and the Coronal Modeling System nonlinear force-free magnetic field reconstruction code, we traced several of the magnetic field lines through the active region. Comparing the spectroscopic and magnetic data, we looked for correlations of the nonthermal velocity with the viewing angle between the line of sight and the magnetic field. We found that nonthermal velocities show a weak anticorrelation with the viewing angle. That is, the tendency is for the nonthermal velocity to be slightly larger in the parallel direction. This parallel broadening may be due to acoustic waves or unresolved parallel flows.

Unified Astronomy Thesaurus concepts: Solar coronal heating (1989); Solar coronal loops (1485); Active solar corona (1988); Quiet solar corona (1992); Solar coronal waves (1995); Solar coronal lines (2038); Ultraviolet spectroscopy (2284)

1. Introduction

Understanding coronal heating is a long-standing problem in solar physics, which is seen most dramatically in active regions, where the temperature and densities are significantly greater than in the quiet-Sun corona. Most theories agree that heating is ultimately driven by fluid motions in the photosphere. Theories differ, though, in how these motions transmit energy to the corona. Nanoflare theories consider the footpoint motions to drive a rearrangement of coronal field lines, which become stressed and then reconnect, releasing energy and heating the corona. Wave-turbulence theories consider the fluid motions to drive waves that travel into the corona, where they drive turbulence and heating. Unfortunately, many commonly used diagnostics for coronal heating, such as temperature, density, differential emission measure (DEM) distribution, and intensity time series, are not able to clearly distinguish between these mechanisms (e.g., Kashyap & Drake 1998; Klimchuk 2015).

Measurements of the nonthermal velocity $v_{\rm nt}$ within the active region coronal loops might provide a new diagnostic for the heating process. These velocities quantify the Doppler broadening of spectral lines, which is caused by unresolved fluid motions. Of particular value is the anisotropy of the nonthermal velocity, that is, the components parallel ($v_{\rm nt,\parallel}$) and perpendicular ($v_{\rm nt,\perp}$) to the mean magnetic field. The utility is that $v_{\rm nt,\perp}$ is thought to be related to wave turbulence, as Alfvén waves cause transverse fluid motions with $v_{\rm nt,\perp}$ proportional to the wave amplitude. Here, we use the term "Alfvén" rather loosely to include both torsional waves and kink modes, which under coronal conditions are nearly incompressible transverse waves that propagate near the Alfvén speed (Goossens et al. 2009). The parallel component may be due to waves or localized heating. One possibility is that slow-mode waves could be produced by mode conversion of kink modes. The resulting waves have velocity perturbations parallel to the magnetic field. Alternatively, any local heating, such as by nanoflares, could drive flows parallel to the loop, thereby increasing $v_{\rm nt,\parallel}$.

Only a few existing measurements have attempted to measure the anisotropy of $v_{\rm nt}$, but the results are ambiguous. Hara & Ichimoto (1999) observed loops at the solar limb and characterized them as being either face-on or edge-on. For face-on loops the line of sight is perpendicular to the magnetic field everywhere, while for edge-on loops the line of sight is perpendicular to the loop near the base and parallel near the loop top. Based on their measurements, Hara & Ichimoto (1999) concluded that line widths were 3–5 km s^{-1} broader in the perpendicular direction than in the parallel direction, so $v_{\rm nt,\perp} > v_{\rm nt,\parallel}$.

A different study appears to have found the opposite result. Hara et al. (2008) measured the center-to-limb variation of $v_{\rm nt}$ for several lines. The relevance to anisotropy is that near the limb the line of sight tends to be perpendicular to the magnetic field, whereas at the disk center the view tends to be along the field. Hara et al. (2008) found broadly overlapping distributions of $v_{\rm nt}$ at both locations, with a slight tendency for $v_{\rm nt}$ to be larger at the disk center. This could be interpreted as weak evidence for $v_{\rm nt,\parallel} > v_{\rm nt,\perp}$. Other studies of center-to-limb variation have not found indications of anisotropy (Del Zanna & Mason 2018).

A limitation of these measurements has been that the angle between the magnetic field and the line of sight is very

uncertain. To overcome this limitation, we have used a nonlinear force-free magnetic field model to extrapolate the magnetic field of the loops and specify their orientation. With this information, we can resolve the uncertainty in the angle between the line of sight and the magnetic field.

Our objective is to determine whether there is a relationship between $v_{\rm nt}$ and the inclination angle of the magnetic field to the line of sight. For our analysis we use observations from Hinode and the Solar Dynamics Observatory (SDO), which are described in Section 2. The analysis of these data to determine the line widths and extrapolate the magnetic field is given in Section 3. Our results are presented in Section 4, along with a discussion of various systematic uncertainties and the interpretation of the results. We present our conclusions in Section 5.

2. Instrument and Observations

We analyzed an active region observed by the Hinode Extreme Ultraviolet Imaging Spectrometer (EIS; Culhane et al. 2007) on 2011 April 19 at 12:03:27 UT. For this observation the 1″ slit of EIS was rastered across the active region spanning from about $x = -101''$ to 118″ in the horizontal direction and from $y = 107''$ to 618″ in the vertical direction. The exposure time for each raster position was about 60 s, so that the data were collected over a total of about 2 hr. The raw data were prepared for further analysis using standard EIS calibration routines to correct for dark current, cosmic rays, and offsets in the wavelength and spatial scales.

The radiometric calibration of EIS has been identified as a potential source of systematic error for line width studies (Brooks & Warren 2016; Testa et al. 2016). This is because over time the EIS sensitivity, parameterized as an effective area, has changed nonuniformly versus wavelength. In order to account for these issues, the line shape analysis described here has been performed without applying the absolute calibration. However, for the DEM analysis, the absolute calibration is needed, and for those results we do apply the effective area calibration as updated by Warren et al. (2014) to account for the wavelength-dependent degradation over time.

As a test, for a few isolated lines we compared the total line widths from the data with and without the absolute calibration. The line widths using the uncalibrated data are smaller by <1% than those based on the calibrated data. For example, the median line width for Fe XV λ284.16 was about 0.0002 Å smaller in the uncalibrated data, which had a median line width was 0.0347 Å. This corresponds to a difference in the median line width of less than 0.2 km s^{-1}. This may also be compared to the typical uncertainty in an individual fit for the Fe XV line width, which was about 0.002 Å. Hence, the systematic difference due to the calibration is only about 10% of the typical fitting uncertainty. Based on these tests, any systematic uncertainties in the line widths due to the absolute calibration are likely negligible. For our analysis we follow Brooks & Warren (2016) and derive line widths from the uncalibrated data.

The magnetic field reconstruction is based on magnetogram data from the Helioseismic Magnetic Imager (HMI; Scherrer et al. 2012) on SDO. We also compare the reconstruction to images from the Atmospheric Imaging Assembly (AIA; Lemen et al. 2012) on SDO in order to verify that the extrapolated magnetic fields resemble the observed magnetic loops. Additionally, we have compared the AIA data to the EIS data in order to co-align the magnetic field model with the EIS spectra.

3. Analysis

Before describing the process in detail, we give a brief outline of the steps in the analysis: We first identified lines dominated by emission from the active region loops, i.e., with minimal contamination from quiet Sun in the foreground or background. For those lines, we subtracted the instrumental broadening and estimated the thermal velocity to extract the nonthermal velocity, $v_{\rm nt}$, and constructed a map of $v_{\rm nt}$ in the observed region. Next, we used a nonlinear force-free field model to extrapolate the photospheric magnetic field into the corona and trace out the active region loops. We traced $v_{\rm nt}$ along these field lines and determined the correlation between $v_{\rm nt}$ and the angle between the magnetic field and the line of sight.

3.1. Spectroscopic Data

All of the EIS data, both calibrated and uncalibrated, were fit with a Gaussian function in order to measure their centroid, line width, and intensity. The main quantity we are interested in is $v_{\rm nt}$, which is derived from the line width. We are interested only in $v_{\rm nt}$ from the active region coronal loops. As the corona is optically thin, the emission for all of the lines is distributed along the line of sight and contains emission from the quiet Sun. In order to avoid lines with a significant quiet-Sun contribution, we identified lines whose emission is mainly coming from the active region.

A common method to restrict the analysis to emission from the active region is to select lines based on their formation temperature. The justification for this is that such hot lines must be emitted from the active region. However, even relatively hot lines can have significant quiet-Sun contributions. For example, Fe XIV has a formation temperature of $\log T_{\rm f} = 6.3$ (here and throughout, temperatures are in K) and is often considered an active region line, but the analysis presented below shows that only 10% of the intensity of this line comes from active region temperatures and the rest is emitted in the quiet Sun.

A more systematic way to constrain the emitting structure is based on a DEM analysis. The DEM, $\phi(T_{\rm e})$, describes the distribution of material along the line of sight as a function of electron temperature, $T_{\rm e}$. The DEM is related to the line intensity of the transition from level j to level i by

$$I_{ji} = \frac{1}{4\pi}\int G_{ji}(T_{\rm e})\phi(T_{\rm e})dT_{\rm e}. \quad (1)$$

Here, $G_{ji}(T_{\rm e})$ is the contribution function and describes the level populations, ionization balance, elemental abundance, and radiative decay rates. The integral is over all temperatures. The needed atomic data are tabulated by the CHIANTI atomic database (Dere et al. 1997; Del Zanna et al. 2021). The DEM can be derived from a set of measured line intensities by inverting Equation (1). Once the DEM is found, the intensity due to emission from material within a given temperature range can be found by integrating Equation (1) over the range of interest. For example, one could define a temperature-based criterion for emission to be from the active region as having the intensity predominantly from material above $\log T_{\rm e} = 6.3$.

To simplify the DEM analysis and the identification of emission sources, we have assumed a relatively simple functional form for the DEM. Our model function assumes that there are several discrete structures along the line of sight corresponding roughly to the transition region, coronal holes, quiet Sun, and active regions. Each of these structures is represented in our parameterization by a delta function with an emission measure amplitude EM_k and a temperature T_k, where the temperatures for the T_k are assumed to fall within a characteristic range. The total DEM is the sum of the contribution from these structures:

$$\phi(T_\mathrm{e}) = \sum_k \mathrm{EM}_k \delta(T_\mathrm{e} - T_k). \tag{2}$$

Although it appears very simple, this function is detailed enough to capture the thermal structure of the emission to the extent permitted by the data. Using a Bayesian analysis, Dere (2022) has shown that observational and atomic physics uncertainties limit the extent to which the DEM can be constrained. Specifically, Dere concluded that four temperature and emission measure pairs were the maximum number of parameters that could be fit without introducing additional assumptions. For example, many emission measure analysis methods make assumptions that the temperature structure should be smooth.

DEM analyses of the solar atmosphere typically show peaks at certain discrete temperatures. Feldman & Landi (2008) argued that DEMs can be considered as having several isothermal components at temperatures of about $\log T_\mathrm{e} \approx 5.75$, 5.95, 6.15, and 6.50, which they identified with emission from the transition region, coronal hole, quiet Sun, and active region, respectively. Dere (2022) found very similar peaks using a different method and with 20 yr of improved atomic data. Our simple model is thus well supported by the observed thermal structure. In any case, for our purposes we need not be concerned whether our discontinuous DEM or a very smooth one is more representative of the real Sun. It suffices that it is representative enough to serve as a criterion for separating the active region emission from background sources.

A practical advantage of this DEM model is that it simplifies much of the analysis. Inserting the functional form of Equation (2) into Equation (1), we can find the DEM by inverting

$$I_{ji} = \sum_k \mathrm{EM}_k G_{ji}(T_k). \tag{3}$$

The inversion was performed using a least-squares fitting algorithm. The free parameters in our model are four EM_k and T_k pairs. In practice, we have performed the fit using $\log(\mathrm{EM}_k)$ and $\log T_k$, since the parameters can vary over orders of magnitude. The data for the fit consisted of 20 emission-line intensities from the ions Fe VIII–XVI, Si VII, Si X, and Ca XV. Model intensities were computed using Equation (3) and compared to these data. The EM_k and T_k parameters were varied iteratively to minimize the squared differences between the data and model intensities. This minimization was performed using the Levenberg–Marquardt least-squares minimization algorithm, as implemented by the IDL *mpfit* routine.

We consider the active region to be the highest-temperature component with $\log T_\mathrm{e} > 6.3$. Denoting this component as the one with $k = \mathrm{AR}$, we can easily find the fraction of emission for a particular line that comes from the active region using

$$f_{\mathrm{AR},ji} = \frac{\mathrm{EM}_{AR} G_{ji}(T_\mathrm{AR})}{\sum_k \mathrm{EM}_k G_{ji}(T_k)}. \tag{4}$$

It is also useful to define a quantity to denote the fraction of the total emission measure coming from the active region, which is given by

$$f_\mathrm{AR} = \frac{\mathrm{EM}_{AR}}{\sum_k \mathrm{EM}_k}. \tag{5}$$

A similar definition could be made for the quiet-Sun contribution or the other components.

This analysis shows that many emission lines that are commonly considered to be formed in the active region are really mainly formed in the quiet Sun. For such lines, the large amount of quiet-Sun material compared to the thin active region loop compensates for a reduced value of $G(T_\mathrm{e})$ in the quiet Sun. For iron ions, we found that the active region contributed about 10% of the emission for Fe XIV λ270.52 (formation temperature $\log T_\mathrm{f} = 6.3$), 50% for Fe XV λ284.16 ($\log T_\mathrm{f} = 6.35$), and 90% for Fe XVI λ262.98 ($\log T_\mathrm{f} = 6.45$). Of these, only the Fe XVI line emission comes predominantly from the active region. Other suitable lines we found were Ca XV λ201.00 ($\log T_\mathrm{f} = 6.65$) with $f_{\mathrm{AR},ji} \approx 100\%$ and Ar XIV λ187.96 ($\log T_\mathrm{f} = 6.55$) with $f_{\mathrm{AR},ji} = 99\%$.

Gaussian profiles were fit to each spectral line in order to determine the line width $\Delta\lambda$. Then, the instrumental broadening, $\Delta\lambda_\mathrm{Inst}$, was subtracted from the total measured line width. Calibrations of $\Delta\lambda_\mathrm{Inst}$ have been given by Young (2011) and by Hara et al. (2011). We have used the calibrations from Hara et al. (2011), which were obtained by cross-calibrating EIS line widths with measurements from ground-based instruments.

After subtracting the instrumental width, the remaining line width comes from physical effects. It is convenient to describe this line width as an effective velocity, defined by

$$v_\mathrm{eff} \equiv \sqrt{\left(\frac{2k_\mathrm{B}T_\mathrm{i}}{M} + v_\mathrm{nt}^2\right)} = \sqrt{v_\mathrm{th}^2 + v_\mathrm{nt}^2}. \tag{6}$$

In our analysis, v_eff comes from the Gaussian fits to the spectral lines corrected for the instrumental broadening. In order to find v_nt, we must subtract the thermal velocity, v_th, which depends on the ion temperature, T_i, and the ion mass M.

For the active region, we have assumed that $T_\mathrm{i} = T_\mathrm{e}$ because the active region loops have a relatively high density, $\approx 10^9$ cm^{-3}, so that collisions between electrons and ions can maintain thermal equilibrium. As we focus on the active region lines, we take this temperature to be the T_AR parameter from our DEM analysis using Equation (2).

The assumption that $T_\mathrm{i} = T_\mathrm{e}$ is also plausible based on the measured v_eff. In the pixels where the active region part of the DEM accounts for more than half of the total emission, that is, $f_\mathrm{AR} > 0.5$, we have found that the average values for v_eff are 33.9 ± 9.2 km s^{-1} for Fe XVI, 42 ± 29 km s^{-1} for Ar XIV, and 51 ± 23 km s^{-1} for Ca XV. Here, the uncertainty represents the standard deviation among the values from each pixel and not

the propagated uncertainty from the Gaussian fits. To test whether the data are consistent with $T_i = T_e$, we considered a less restrictive assumption: that T_i is the same for all the ions but may differ from the T_e. This is less restrictive because of the large mass difference between ions and electrons, which causes collisions to couple the ion temperatures more strongly to one another and to the protons than to the electrons. Under this assumption, we can perform a fit to Equation (6) with the ion mass M as the dependent variable and T_i and v_{nt} as free parameters. A least-squares fit finds that $\log T_i = 6.6 \pm 4.0$. This average value matches the T_e expected for an active region. Clearly there is a huge uncertainty, which is partly due to the spread in v_{eff} throughout the active region, but more importantly to the extremely limited range of masses for these three ions. In particular, Ca and Ar have nearly the same ion mass.

In order to account for the uncertainties in v_{eff} and T_{AR} when obtaining v_{nt}, we have used a Monte Carlo−type approach. We drew normally distributed random numbers with means equal to the values inferred from the measurements of v_{eff}, and $\log T_{AR}$, and with the standard deviations of those random number distributions equal to the measurement uncertainties for v_{eff} and $\log T_{AR}$. These distributions sample from probability distributions for each of these quantities. We computed v_{nt} for each sampled pair using Equation (6). About 5000 samples were used to derive the probability distribution for v_{nt}. In some cases a sampled pair of line width and temperature produces an unphysical value with $v_{nt} < 0$. Such values were ignored based on the prior assumption that the probability of a negative nonthermal velocity is zero. In order to represent v_{nt} at each location with a single value and an uncertainty, we have used the median of the positive v_{nt} distribution. For the uncertainty, we computed the range about the median that would contain 68.2% of the probability distribution, analogous to the 1σ range. The range was roughly symmetric above and below the median, so we take half that range as an estimate of the 1σ uncertainty.

We find that the median v_{nt} in the active region based on the Fe XVI line is typically $v_{nt} = 20 \pm 15$ km s^{-1}. This value is consistent with other measurements for v_{nt}, which have found values in the range of 10–20 km s^{-1} in active regions (e.g., Imada et al. 2009; Brooks & Warren 2016). For Ca XV and Ar XIV lines, though, we find systematically higher values with $v_{nt} = 57 \pm 33$ km s^{-1} and $v_{nt} = 74 \pm 30$ km s^{-1}, respectively. These greater values are due to the larger uncertainties in the measurements of the weaker Ca XV and Ar XIV lines compared to the strong Fe XVI line.

Our method for subtracting the thermal velocity inflates the inferred value of v_{nt} at locations where there are large uncertainties. This is because v_{nt} is bounded below by zero, but there is no upper bound. When the uncertainties in v_{eff} or T_{AR} are large, the probability distribution for v_{nt} is relatively flat and extends over a broad range. As a result, the median value for v_{nt} can become very large and proportional to the uncertainties. In order to mitigate this problem, we have limited our analysis to locations deep in the active region where the high-temperature emission is strongest, as discussed in Section 4. Additionally, we rely for our analysis mainly on the more reliable Fe XVI, while using the weaker lines in a supporting role as a check for consistency.

3.2. Magnetic Field Reconstruction

The angle θ between the line of sight and the magnetic field of the loop is found from magnetic field extrapolation, which is performed using the Coronal Modeling System (CMS; van Ballegooijen 2004; Asgari-Targhi & van Ballegooijen 2012; Asgari-Targhi et al. 2021). We used line-of-sight magnetogram data from HMI, which provides full-disk magnetograms with 0.″5 resolution and a 45 s cadence (Scherrer et al. 2012). Our CMS-modeled magnetic field is also constrained by extreme-ultraviolet (EUV) images. These data are taken from AIA (Lemen et al. 2012).

To model the coronal magnetic field, we first computed the potential field (i.e., the field with current density $J = 0$) for the active region. To construct a potential magnetic field model of this active region, we used the HMI magnetogram and the HMI synoptic map for Carrington rotation 2019. The calculation is performed on a high-resolution domain surrounding the target region, and a global potential field model is used to set the boundary conditions. We compared this model to images from AIA and assessed that the potential model was insufficient to match the observed coronal loops. This is due to currents present in the active region that are neglected in the potential field model. We take these currents into account by using magnetofrictional relaxation to produce a nonlinear force-free field (NLFFF).

In a force-free nonpotential field, the electric current flows parallel to the magnetic field, and so the Lorentz force vanishes, $\boldsymbol{J} \times \boldsymbol{B} = 0$. In this study, deviations from the potential field model were present due to the existence of a filament in the region. Therefore, we applied the NLFFF model, where these deviations were corrected by introducing an untwisted flux bundle with an axial flux of 10^{20} Mx and a poloidal flux of 10^{9} Mx (see Bobra et al. 2008, for details). We then applied magnetofrictional relaxation (Yang et al. 1986; van Ballegooijen et al. 2000). After 90,000 iterations an NLFFF model was obtained. The parameters of the magnetic flux bundle were constrained by visually comparing the final extrapolated magnetic fields to the AIA EUV images. Based on this comparison, CMS provides accurate orientations of the coronal magnetic fields that are consistent with both the magnetogram data and the observed coronal loops. More details about CMS can be found in the references with examples of its successful application to studies of filaments (van Ballegooijen 2004), active regions (Bobra et al. 2008; Su et al. 2009a, 2009b, 2011), X-ray sigmoids (Savcheva & van Ballegooijen 2009), and other loops (Asgari-Targhi & van Ballegooijen 2012; Asgari-Targhi et al. 2013, 2014).

The magnetic field reconstructions were co-aligned to the spectra by comparing the EIS Fe XII λ195.12 line emission with the 193 Å channel of AIA, for which the emission is primarily from the same ion. Once co-aligned, we projected the magnetic field lines onto the plane of sky and associated each EIS pixel with the corresponding point on the field line lying along the same line of sight. Figure 1 shows selected magnetic field lines computed by CMS superimposed on an image in the Fe XII λ195.12 line measured by EIS. Fe XII formation peaks at relatively cool temperatures ($\log T_f = 6.2$), but its contribution function extends into the active region temperature range and the emission from the denser active region loops enhances the intensity above the background level, rendering the loops visible. Figure 2 shows the region using the intensity of the

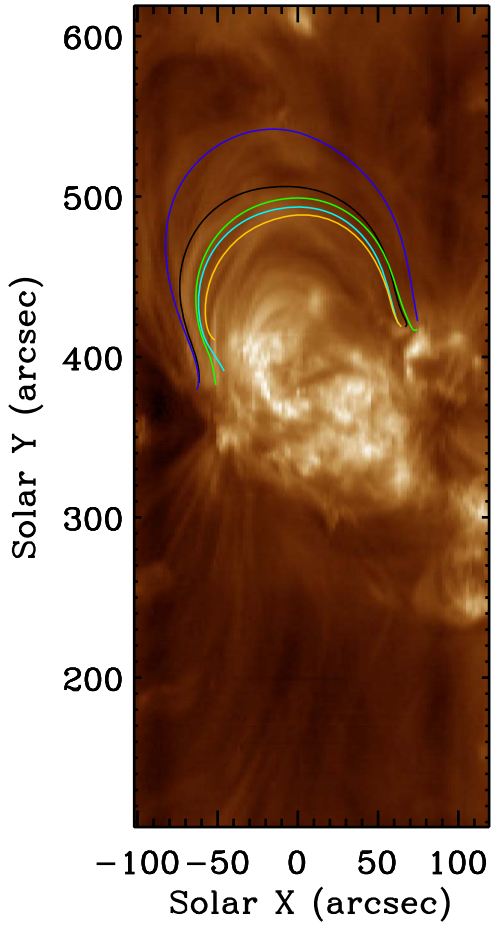

Figure 1. Image of the intensity of the Fe XII λ195.12 line measured by EIS for this observation. The colored curves show the selected magnetic field lines traced by the CMS magnetic field extrapolation superimposed on the EIS data.

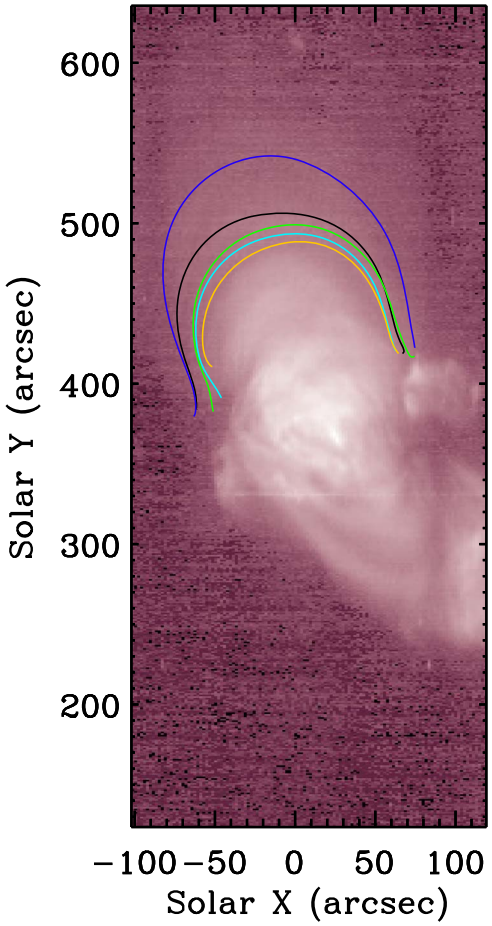

Figure 2. Same as Figure 1, but in the Fe XVI λ262.98 line.

Fe XVI λ262.98 line, which is dominated by emission from the active region at high temperatures ($\log T_f = 6.45$).

The CMS reconstruction provides the three-dimensional vector magnetic field throughout the corona. Magnetic field lines, such as those in Figure 1, are traced out using this model. Thus, CMS provides the coordinates of the magnetic field lines and the vector magnetic field at each point along the traced field lines. For each spatial pixel in the EIS spectra along the loop, we found the angle between the magnetic field and the line of sight. In the CMS coordinate system the $\hat{z}$-direction is the line of sight, so the angle between the magnetic field and the line of sight is $\theta = \cos^{-1}(B_z/B)$, where B is the magnitude of the magnetic field strength.

4. Results and Discussion

We looked for correlations between v_{nt}, v_{eff}, and θ for all the points along the five traced coronal loops. One systematic correlation that we need to control for is the influence of noise in the measurements of v_{eff}. As discussed above, we were focusing on lines from Fe XVI, Ca XV, and Ar XIV because their intensities are dominated by active region plasma. Outside of the active region, these lines are very weak, and the line widths have a large uncertainty. As discussed above, since v_{nt} cannot be less than zero, the uncertainty propagation will tend to increase the statistical median value of the derived v_{nt} in regions where the lines are weak. In order to mitigate these correlations, we limit the analysis to regions where the active region contributes at least half of the total emission measure $f_{AR} > 0.5$. Figure 3 maps f_{AR} in this region.

In the following discussion, we quantify correlations between variables using the Spearman rank correlation coefficient ρ_c. This measure of correlation is based on the ranking of the two variables so that any perfect monotonic correlation has $\rho_c = 1$ and a perfect monotonic anticorrelation has $\rho_c = -1$. Significance for the Spearman correlation is determined by finding the probability that the data would result in a value of ρ_c equal to or larger than the computed value if the null hypothesis that the data are in fact uncorrelated were true, and then the significance is the complementary probability to that. That is, we say that the statistic is 99% significant if there is a probability of $\leqslant$1% that the data are consistent with the null hypothesis. In the following, all correlations are significant at least the 99% level or better unless specifically noted otherwise.

Figure 4 illustrates the relationship between v_{nt} and θ for the Fe XVI λ262.98 line. For this line, the Spearman correlation coefficient, ρ_c, was statistically significant with $\rho_c = -0.35$. The analysis based on Ca XV λ201.00 agreed with $\rho_c = -0.29$. We also performed the analysis for the Ar XIV λ187.96 line, which showed a weaker correlation of $\rho_c = -0.14$ that was also less significant at 98%. The correlation is likely weaker because the Ar XIV line has a lower intensity than either of the other two lines, and the resulting uncertainty in the measured line widths obscures the correlation. For all three emission lines, the correlations and significance levels remained about

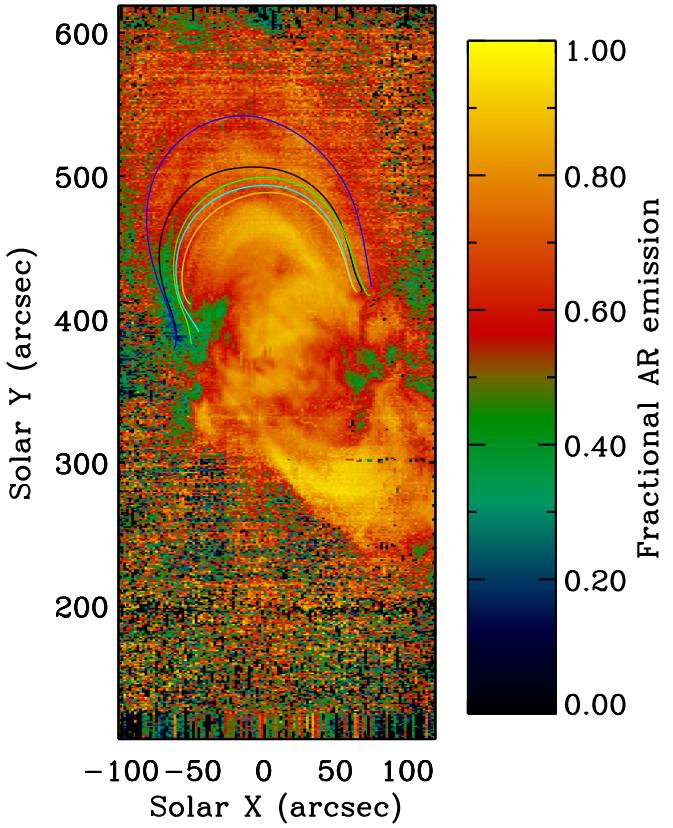

Figure 3. Map of $f_{\rm AR}$ throughout the EIS observation, showing the fraction of the emission measure in each pixel that comes from the active region component of the DEM. The colored curves show the selected magnetic field lines from Figure 1 superimposed on the EIS data.

the same if we raised the threshold criterion to $f_{\rm AR} = 0.6$. Overall, there is a weak tendency for $v_{\rm nt}$ to be greater in the direction parallel to the loop magnetic field.

We have also looked for correlations between $v_{\rm eff}$ and θ. Doing so may obviate any systematic uncertainties introduced by the subtraction of the thermal width, but at the expense of making correlations by not correcting for the ion temperature dependence. We found that the correlations with $v_{\rm eff}$ tend to be weaker and less significant than with $v_{\rm nt}$ itself. For Fe XVI, the Spearman correlation coefficient $v_{\rm eff}$ and θ are not statistically significant when the threshold is $f_{\rm AR} > 0.5$. With a more restrictive criterion of $f_{\rm AR} > 0.6$, we find a correlation coefficient of -0.12. For Ca XV, $v_{\rm eff}$ shows a weak inverse correlation with θ having $\rho_{\rm c} = -0.13$. The Ar XIV data showed no significant correlations. Hence, we find that for $v_{\rm eff}$ the inverse correlation between $v_{\rm eff}$ and θ probably exists but is weaker than for $v_{\rm nt}$.

We can readily estimate the magnitude of the perpendicular $v_{\rm nt,\perp}$ by taking the average $v_{\rm nt}$ value for those pixels with large angles. Here, we focus on the Fe XVI line, since it is the brightest line with the smallest uncertainties. For the range $\theta = 80°$–$90°$, we find that the average $v_{\rm nt,\perp} = 22 \pm 11$ km s^{-1}. It is more difficult to estimate the parallel $v_{\rm nt,\parallel}$ since there are very few lines of sight in this observation that view the loop at a small nearly parallel angle. One possibility is to extrapolate to small angles by performing a fit to the data using (Hahn & Savin 2013)

$$v_{\rm nt} = \sqrt{v_{\rm nt,\parallel}^2 \cos^2\theta + v_{\rm nt,\perp}^2 \sin^2\theta}. \quad (7)$$

Such a fit yields (Figure 5) $v_{\rm nt,\parallel} = 28 \pm 3$ km s^{-1} and $v_{\rm nt,\perp} = 19.0 \pm 0.3$ km s^{-1}. These uncertainties are probably underestimates, as they are weighted by the uncertainties of each pixel but ignore possibly real pixel-to-pixel variations. Moreover, due to the zero lower bound on $v_{\rm nt}$ discussed above, these magnitudes are likely systematically overestimated.

We can estimate the energy flux in the loop due to the parallel and perpendicular nonthermal velocities if we interpret them as the amplitudes of slow magnetosonic waves and Alfvén waves, respectively. In that case, the energy flux of the waves is approximately $F \approx \rho v_{\rm nt}^2 T_{\rm g}$, where ρ is the mass density and $T_{\rm g}$ is the appropriate group velocity of either the sound speed or the Alfvén speed, respectively. Given the temperatures, densities, and magnetic fields of these loops, slow-mode waves would propagate at about the sound speed with $c_s \approx 300$ km s^{-1}, and the Alfvén speed is $V_{\rm A} \approx 1000$ km s^{-1}. Using the above nonthermal velocities and an estimated density of 10^9 cm^{-3}, the energy fluxes for slow-mode waves would be about $F_{\rm s} \approx 400$ W m^{-2} and for Alfvén waves $F_{\rm A} \approx 600$ W m^{-2}. This suggests that there is a similar amount of energy in the parallel and perpendicular fluctuations.

It is implicit in the above analysis that $v_{\rm nt}$ and its components do not vary along the loop. This assumption is unavoidable, as there are not enough measurables to extract possible actual variations in $v_{\rm nt,\perp}$, $v_{\rm nt,\parallel}$, and $T_{\rm i}$ simultaneously. This assumption is also made in other studies, such as Hara & Ichimoto (1999) and Hara et al. (2008) mentioned in the Introduction. Here, we have investigated some factors that might limit the validity of this assumption by examining how the parameters of interest vary with distance along the loop.

For this observation, we are looking down onto the loop so that the viewing angle is most parallel near the footpoints. Because of this perspective, the legs of the loop are greatly foreshortened and cover only a few pixels. This is illustrated in Figure 6, where we have plotted the viewing angle θ as a function of distance from the center of the loop normalized by the loop half length, s. That is, the center of the loop is at $s = 0$, and the footpoints are at $s = 1$.

The temperature $T_{\rm AR}$ has an inverse correlation with s, though it is quite weak with a correlation coefficient of only $\rho_{\rm c} = -0.15$. A decreasing temperature toward the footpoints is theoretically expected for active region loops (e.g., Rosner et al. 1978). One possible reason for the weak correlation here is our assumption that lower temperatures are due to quiet-Sun contamination. It is possible that we are misinterpreting some positions near the loop footpoints as reflecting quiet-Sun background, when those positions are actually viewing emission from the cooler part of the loop.

One might be concerned whether the subtraction of the thermal width from $v_{\rm eff}$ could introduce a systematic effect that would bias the $v_{\rm nt}$ data due to the above correlation between temperature and s. Since a weak anisotropy is observed also in $v_{\rm eff}$, the stronger correlation with $v_{\rm nt}$ suggests that $v_{\rm nt}$ really is varying and we have subtracted the thermal width that was obscuring that correlation when looking at $v_{\rm eff}$.

It is possible that the measured correlation with $v_{\rm nt}$ is not caused by anisotropy directly, but rather that the apparent correlation between $v_{\rm nt}$ and θ could be an artifact of an underlying real relationship with distance along the loop from a footpoint. However, the relationship between position along the loop, s, and θ is not monotonic (see Figure 6). Rather, θ varies significantly within the range of about 60°–90° over a large fraction of the loop

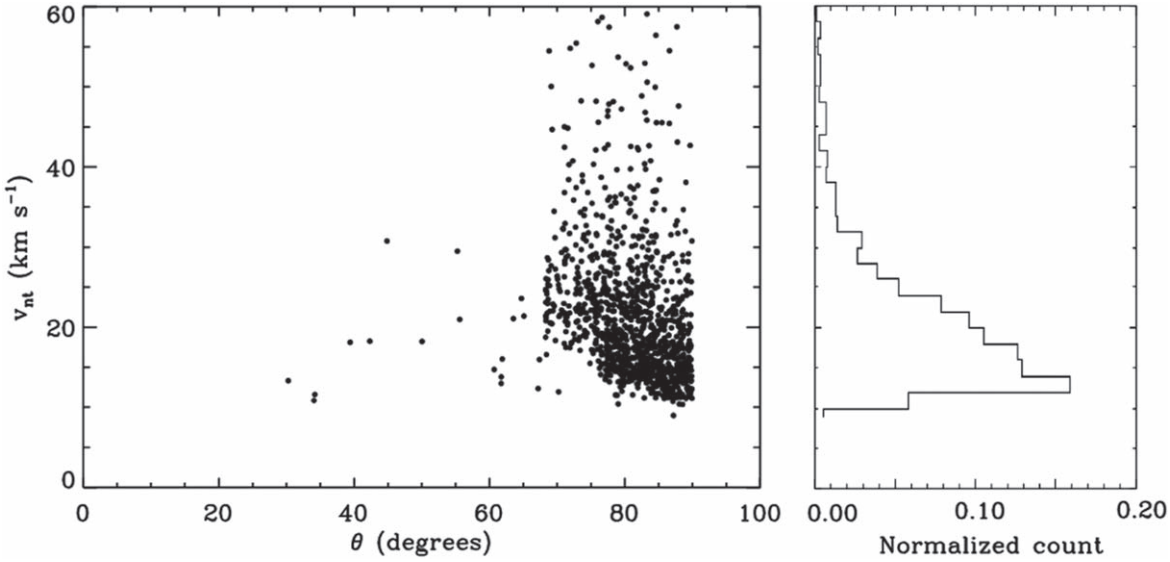

Figure 4. Composite of v_{nt} vs. θ for Fe XVI points drawn from all of the traced loops that satisfy the criteria that $f_{AR} \geqslant 0.5$. Because of the zero lower bound, large v_{nt} values can occur at locations where there is more uncertainty in v_{eff} or T_{AR}. The histogram on the right helps to illustrate the number of such outliers compared to the bulk of the v_{nt} distribution.

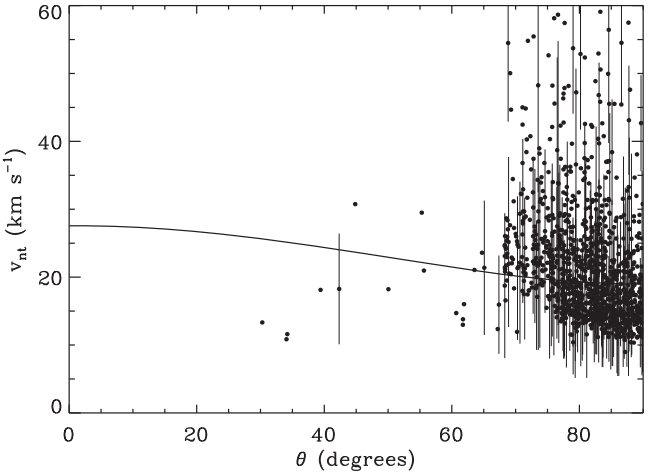

Figure 5. Fit to the v_{nt} vs. θ data from Fe XVI. The data points are the same as those in Figure 4. Error bars are drawn on every 10th point to illustrate the 1σ uncertainties. The solid line indicates the fit to the data using Equation (7), which estimates $v_{nt,\parallel} = 28 \pm 3$ km s^{-1} and $v_{nt,\parallel} = 19.0 \pm 0.3$ km s^{-1}.

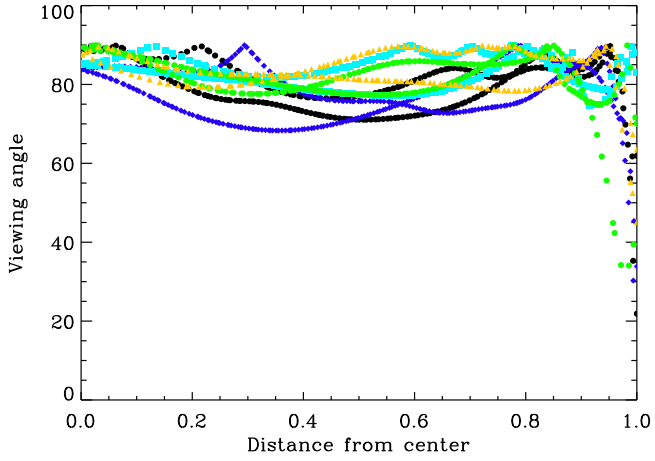

Figure 6. Angle θ between the line of sight and the loop magnetic field as a function of the normalized distance from the loop center for the five traced loops. The different symbols and colors indicate different loops. The colors match those in Figure 1.

length, and small angles are only seen very close to the footpoints. Consequently, the observed correlations of v_{nt} with angle are mostly decoupled from any variations with s, although there was a weak, but significant, correlation between v_{nt} and s with $\rho_c = -0.11$ based on the Fe XVI data. This correlation is weaker than that between v_{nt} and θ, so it is likely that the observed correlations are mainly due to anisotropy.

5. Conclusion

We have measured the variation of v_{nt} along active region coronal loops and compared those measurements to the viewing angle of the line of sight with respect to the magnetic field direction, θ. This analysis is made possible by a nonlinear force-free field extrapolation to infer the magnetic field direction. Additionally, we found that background emission from the quiet Sun is strong, so that only a few lines with very high formation temperature are actually dominated by the active region.

Our results suggest that there is a weak but significant negative correlation between v_{nt} and θ. One interpretation is that the v_{nt} is anisotropic with $v_{nt,\parallel} > v_{nt,\perp}$. However, this interpretation relies on the assumption that v_{nt} and its components are constant along the loop, so that the variations can be ascribed to the viewing angle and anisotropy. This is a common assumption made by other groups in previous studies of v_{nt} in active regions.

In future measurements, we would like to better test this assumption by studying active regions with loops that have a nearly constant viewing angle and thereby resolve whether the changes in v_{nt} are due to anisotropy or distance along the loop. There are a number of reasons that v_{nt} might vary along the loop. Wave amplitudes might be smaller near the footpoints due to the larger density there and grow in amplitude as the density decreases, or the amplitudes might be larger near the footpoints close to the excitation source and decrease due to dissipation as they travel up the loop, or the fraction of

compressive waves that contribute to $v_{nt,\parallel}$ or Alfvén waves that contribute to $v_{nt,\perp}$ might also vary with s.

Another limitation of these data is that the range of θ along the loop was limited to rather steep angles. For an active region near disk center, the line of sight is looking down onto the loop. As such, the vertical legs of the loop where the line of sight is nearly parallel to the line of sight are foreshortened, and the legs are covered by only a few spatial pixels. Most of the field of view observes the region near the top of the loop where the line of sight is close to perpendicular. The anisotropy of v_{nt} would be better constrained by using observations that span a greater range of θ.

In order to help resolve these issues of variation along the loop and the limited dynamic range of angles, we plan to analyze an observation at the solar limb. At the limb, we expect to observe face-on and edge-on loops, much as was seen by Hara & Ichimoto (1999), but with the advantage of using our improved magnetic field diagnostics to remove the ambiguity as to the actual magnetic field direction.

Acknowledgments

This work was supported by the NASA Heliophysics Guest Investigator program grant 80NSSC20K0692.

ORCID iDs

Michael Hahn https://orcid.org/0000-0001-7748-4179
Mahboubeh Asgari-Targhi https://orcid.org/0000-0003-0204-8385
Daniel Wolf Savin https://orcid.org/0000-0002-1111-6610

References

Asgari-Targhi, M., Golub, L., Hahn, M., Karna, N., & Savin, D. W. 2021, ApJ, 910, 113
Asgari-Targhi, M., & van Ballegooijen, A. A. 2012, ApJ, 746, 81
Asgari-Targhi, M., van Ballegooijen, A. A., Cranmer, S. R., & DeLuca, E. E. 2013, ApJ, 773, 111
Asgari-Targhi, M., van Ballegooijen, A. A., & Imada, S. 2014, ApJ, 786, 28
Bobra, M. G., van Ballegooijen, A. A., & DeLuca, E. E. 2008, ApJ, 672, 1209
Brooks, D. H., & Warren, H. P. 2016, ApJ, 820, 63
Culhane, J. L., Harra, L. K., James, A. M., et al. 2007, SoPh, 243, 19
Del Zanna, G., Dere, K. P., Young, P. R., & Landi, E. 2021, ApJ, 909, 38
Del Zanna, G., & Mason, H. E. 2018, LRSP, 15, 5
Dere, K. 2022, ApJ, 930, 86
Dere, K. P., Landi, E., Mason, H. E., Fossi, B. C. M., & Young, P. R. 1997, A&AS, 125, 149
Feldman, U., & Landi, E. 2008, PhPl, 15, 056501
Goossens, M., Terradas, J., Andries, J., Arregui, I., & Ballester, J. L. 2009, A&A, 503, 213
Hahn, M., & Savin, D. W. 2013, ApJ, 763, 106
Hara, H., & Ichimoto, K. 1999, ApJ, 513, 969
Hara, H., Watanabe, T., Harra, L. K., et al. 2008, ApJ, 678, 67
Hara, H., Watanabe, T., Harra, L. K., Culhane, J. L., & Young, P. R. 2011, ApJ, 741, 107
Imada, S., Hara, H., & Watanabe, T. 2009, ApJ, 705, 208
Kashyap, V., & Drake, J. J. 1998, ApJ, 503, 450
Klimchuk, J. A. 2015, RSPTA, 373, 20140256
Lemen, J. R., Title, A. M., Akin, D. J., et al. 2012, SoPh, 275, 17
Rosner, R., Tucker, W. H., & Vaiana, G. S. 1978, ApJ, 220, 643
Savcheva, A., & van Ballegooijen, A. A. 2009, ApJ, 703, 1766
Scherrer, P. H., Schou, J., Bush, R. I., et al. 2012, SoPh, 275, 207
Su, Y., Surges, V., van Ballegooijen, A., DeLuca, E., & Golub, L. 2011, ApJ, 734, 53
Su, Y., van Ballegooijen, A., Lites, B. W., et al. 2009a, ApJ, 691, 105
Su, Y. N., van Ballegooijen, A. A., Schmieder, B., et al. 2009b, ApJ, 704, 341
Testa, P., De Pontieu, B., & Hansteen, V. 2016, ApJ, 827, 99
van Ballegooijen, A. A. 2004, ApJ, 612, 519
van Ballegooijen, A. A., Priest, E. R., & Mackay, D. H. 2000, ApJ, 539, 983
Warren, H. P., Ugarte-Urra, I., & Landi, E. 2014, ApJS, 213, 11
Yang, W. H., Sturrock, P. A., & Antiochos, S. K. 1986, ApJ, 309, 383
Young, P. 2011, Instrumental Line Widths for the Narrow Slits of EIS, Version 0.1 EIS Software Note No. 7, available at: ftp://sohoftp.nascom.nasa.gov/solarsoft/hinode/eis/doc/eis_notes/07_LINE_WIDTH/eis_swnote_07.pdf